International Journal of Hydrogen Energy 205 (2026) 153321

Contents lists available at ScienceDirect

International Journal of Hydrogen Energy

journal homepage: www.elsevier.com/locate/he

Laser-engineered Inconel 625 for enhanced oxygen evolution electrocatalysis

Angelja Kjara Surca [a,*], Marjan Bele [a], Črtomir Donik [b], Irena Paulin [b], Martin Šala [c], Jakob Starec Oman [a], Miha Osredkar [a], Mejrema Nuhanović [a], Jan Ocepek [a], Matjaž Godec [b], Goran Dražič [a], Nejc Hodnik [a,b], Luka Suhadolnik [a,**]

[a] Department of Materials Chemistry, National Institute of Chemistry, Hajdrihova 19, SI-1000 Ljubljana, Slovenia
[b] Institute of Metals and Technology, Lepi pot 11, SI-1000 Ljubljana, Slovenia
[c] Department of Analytical Chemistry, National Institute of Chemistry, Hajdrihova 19, SI-1000 Ljubljana, Slovenia

ARTICLE INFO

Keywords:
Inconel 625
Laser surface engineering
Electrocatalysis
Oxygen evolution reaction
Water splitting

ABSTRACT

The oxygen evolution reaction (OER) is a major bottleneck in electrochemical water splitting due to its sluggish kinetics and high overpotentials. Here, we report a single-step laser surface engineering approach to convert commercial Inconel 625 alloy into an active OER electrocatalyst. Pulsed laser treatment generates a hierarchical, "cauliflower-like" nanostructure that significantly enhances the electrochemically active surface area. Electrochemical testing in 1 M KOH shows that the laser-treated surface achieves an overpotential of 270 mV at 10 mA cm^{-2}, corresponding to a 30 mV cathodic shift relative to the untreated alloy. During electrochemical activation, selective dissolution of Mo and Cr produces a Ni-rich surface that facilitates the formation of catalytically active γ-NiOOH species. Raman spectroscopy confirms γ-NiOOH formation with characteristic bands at 470 and 548 cm^{-1}, while the shoulders at 493 and 539 cm^{-1} suggest Fe incorporation into the oxyhydroxide structure. Under OER conditions, we also detect low-intensity bands in the spectral region between 800 and 1150 cm^{-1}, which we ascribe to Ni-OO^{-} species stabilized by cations. The Tafel slope decreases from 59.9 mV dec^{-1} for pristine Inconel 625 to 39.2 mV dec^{-1} after laser-treatment and electrochemical conditioning. Identical location SEM technique is used to follow how the hierarchical structure of the laser-treated sample partly coalesce and locally flatten after the electrochemical treatment. These results demonstrate that laser surface engineering provides a scalable and effective strategy to transform robust industrial alloys into functional OER electrocatalysts, offering new avenues for cost-effective water-splitting technologies.

1. Introduction

Electrocatalytic water splitting is a key technology on the way to sustainable hydrogen production [1]. In particular, the oxygen evolution reaction (OER) remains a major kinetic bottleneck due to its sluggish multi-electron transfer mechanism. While noble metal oxides such as IrO_2 and RuO_2 exhibit the highest OER activity among known materials, their high cost and scarcity hinder their use on a large-scale. This has led to intensive research into non-noble, earth-abundant transition metals, particularly Ni, Co, and Fe, as promising alternatives for alkaline electrocatalysis [1,2].

Ni is of particular interest due to its ability to form catalytically active Ni-oxyhydroxide species under anodic conditions [3,4]. Its performance can be further enhanced by elements such as Fe and Co, which modify the electronic structure and facilitate charge transfer [5,6]. In addition to compositional tuning, surface nanostructuring has emerged as a key strategy for increasing the number of accessible active sites and improving mass transport. Among the various methods explored, laser-based surface engineering offers a straightforward, fast, and scalable approach to create large-surface-area catalyst surfaces. Recent applications include the preparation of laser-induced high-entropy alloys for seawater splitting [7] and laser-structured Ni surfaces for the hydrogen evolution reaction (HER) [8]. However, their application in the development of OER catalysts remains largely underexplored.

A wide range of synthetic routes has also been used to obtain

* Corresponding author.
** Corresponding author.
E-mail addresses: angelja.k.surca@ki.si (A.K. Surca), luka.suhadolnik@ki.si (L. Suhadolnik).

https://doi.org/10.1016/j.ijhydene.2025.153321
Received 19 August 2025; Received in revised form 27 November 2025; Accepted 28 December 2025
Available online 7 January 2026

nanostructured transition-metal oxides and hydroxides for electrocatalytic applications, including sol-gel synthesis [9], chemical vapor deposition (CVD) [10], electrodeposition [11], and hydrothermal processing [12]. Each of these techniques allows a certain degree of control over composition and morphology, yet they also exhibit specific drawbacks. The sol-gel method often requires precise control of pH, temperature, and ageing to achieve reproducible results, while CVD demands high-temperature conditions and specialized equipment. Electrodeposition and hydrothermal synthesis, although widely used, rely on chemical precursors and long processing times, which can complicate scaling to large, conductive metallic substrates. Moreover, these methods typically modify the surface by adding external material rather than directly transforming the existing alloy itself.

In contrast, laser-based surface modification offers a powerful means of tailoring surface structure and composition through localized melting and rapid solidification. Widely employed in fields such as corrosion protection, tribology, and functional coatings, techniques like laser remelting, cladding, and texturing have been used to enhance surface durability and reactivity [13,14]. These methods enable the formation of finely structured surface layers with unique morphological and chemical features. Despite their maturity in materials engineering, laser-based approaches are only gradually finding their place in electrocatalysis, where they remain largely underutilized for rational catalyst design. Motivated by this gap, we explored how a controlled laser processing protocol, rarely applied in the fabrication of electrocatalysts [15,16], modifies the surface morphology and chemical state of a commercial Ni-based alloy, and how these changes affect its oxygen evolution performance in alkaline media.

Among the various commercially available Ni-based alloys, Inconel 625 stands out due to its excellent mechanical strength, thermal stability, and corrosion resistance in aggressive environments [17,18]. It is widely used in the aerospace, marine, and chemical processing industries, particularly in components exposed to high temperatures, pressure, and corrosive media. These demanding applications are made possible by the alloy's multicomponent composition, which includes Fe, Cr, Mo, and Nb, each contributing to its structural integrity and chemical durability.

Beyond its industrial relevance, Inconel 625 presents an appealing substrate for surface engineering: it is widely available, mechanically robust, and chemically versatile, making it well suited for research into complex surface transformations. For example, laser peening studies of Inconel 625 have demonstrated that laser treatment conditions can either improve or degrade the corrosion properties of this material [19]. Although its electrochemical stability has been extensively studied for corrosion protection applications, its behavior under electrocatalytic conditions remains largely unexplored. Furthermore, to our knowledge, laser-based surface modification has not yet been applied as a single-step method to transform Inconel 625 into an active electrocatalyst.

In this study, we performed a single-step laser treatment of Inconel 625 to induce controlled surface nanostructuring and compositional redistribution. The goal was to investigate how laser irradiation modifies the microstructure and chemical state of this complex, multicomponent alloy, both immediately after processing and after the exposure to OER electrochemical conditions in 1 M KOH. A comprehensive set of characterization techniques, including identical location scanning electron microscopy (IL-SEM) and energy-dispersive X-ray spectroscopy (EDXS) mapping, transmission electron microscopy (TEM), X-ray diffraction (XRD), X-ray photoelectron spectroscopy (XPS), time-of-flight secondary ion mass spectrometry (ToF-SIMS) and mimicked *in situ* Raman spectroscopy, was employed to examine morphological and chemical changes across different scales and relate them to material transformation pathways. This work provides fundamental insights into the surface evolution and electrocatalytic properties of Inconel 625 upon combined laser and electrochemical treatments, offering a framework for its rational utilization in future functional applications.

2. Experimental section

2.1. Catalyst preparation

Laser treatment. The surface modification of Inconel 625 was performed using a pulsed Yb-doped fiber laser system (20 W, Gweike) operating at 1064 nm. The laser delivered pulses at a frequency of 20 kHz with an average power output of 16 W. The beam was aligned perpendicular to the sample surface, with a working distance of 261 mm. Laser scanning was carried out using a line spacing of 10 μm and a scanning speed of 500 mm s^{-1}, enabling homogeneous surface structuring over the treated area.

2.2. Catalyst characterization techniques

IL-SEM, IL-SEM–EDXS, and IL–EDXS mapping analyses. Identical location scanning electron microscopy (IL-SEM) and energy-dispersive X-ray spectroscopy (EDXS) were performed using a ThermoFisher Apreo 2S scanning electron microscope (Thermo Fisher Scientific, The Netherlands) equipped with an Ultim Max 100 EDXS detector (Oxford Instruments, UK).

TEM and STEM images were acquired using a Cs-corrected scanning transmission electron microscope, JEOL ARM 200 CF, operated at 80 keV to reduce the effects of the electron beam on the sample. For chemical analysis, a Jeol Centurio EDXS system with a 100 mm^2 SDD detector and a Gatan Quantum ER double EELS spectrometer were used.

XRD analysis. The phase composition of the starting alloy and laser-treated surface was analyzed by X-ray diffraction using a PANalytical X'Pert 3040 diffractometer equipped with a rotating copper anode (Cu Kα radiation: $\lambda_1 = 1.54059$ Å, $\lambda_2 = 1.54441$ Å). The instrument operated at an accelerating voltage of 40 kV and a current of 45 mA. The diffraction patterns were collected in the 2θ range from 20° to 100° with a step size of 0.02°, using a linear detector. To minimize preferred orientation effects, samples were continuously rotated during data acquisition, with the laser-treated surface facing the incident beam.

XPS analysis. X-ray photoelectron spectroscopy (XPS) was performed with the Supra + device (Kratos, Manchester, UK) equipped with a monochromatic Al Kα source (photon energy 1486.6 eV). Prior to analysis, all samples were fixed to the sample holder using silicone-free, double-sided adhesive tape. The spectra were acquired at a take-off angle of 90°, targeting a sample area of 300 μm by 700 μm. The chamber base pressure was maintained below $2 \bullet 10^{-9}$ mbar during acquisition. High-resolution core-level spectra were acquired at a pass energy of 20 eV. All binding energies were referenced to the C 1s peak corresponding to C–C/C–H at 284.8 eV. Data acquisition and processing were performed with ESCApe 1.5 software.

ToF-SIMS analysis. Time-of-flight secondary ion mass spectrometry (ToF-SIMS) measurements were conducted using an M6 instrument (IONTOF GmbH, Münster, Germany) operated in negative ion mode. The sample was mounted onto a stainless-steel holder using silicone-free, double-sided adhesive tape. The pressure in the analysis chamber was below $5 \bullet 10^{-10}$ mbar throughout the measurements. The surface analysis was carried out using a pulsed 30 keV Bi^+ primary ion beam, rastered over a central area of 300 μm by 300 μm within a larger sputter crater. Sputtering was performed with a 2 keV Cs^+ ion beam over an area of 500 μm × 500 μm for 3 h. The Cs^+ ion source was preconditioned for several hours prior to measurement to ensure beam current stability. Mass calibration was performed using characteristic peaks of known Ni-related species. Data collection and processing were carried out using the SurfaceLab 7.5 software (IONTOF).

ICP-OES analysis. The samples for the determination of the metal concentrations were collected from the 1 M KOH electrolyte after the electrochemical cycling and analyzed using optical emission spectrometry with inductively coupled plasma. All reagents used were of analytical grade or better. For sample dilution and preparation of standards, ultrapure water (18.2 MΩ cm, Milli-Q, Millipore) and ultrapure

acid (HNO_3, Merck-Suprapur) were used. The standards were prepared by dilution of certified, traceable, inductively coupled plasma (ICP)-grade single-element standards (Merck CertiPUR). A Varian 715-ES ICP optical emission spectrometer was used. Prior to analysis, samples were diluted with 2 %V/V HNO_3 as required.

Electrochemical analysis. The electrochemical tests were carried out at room temperature using a custom-built single-compartment Teflon cell in a three-electrode configuration. The laser-treated Inconel 625 sample, embedded in a Teflon holder, served as the working electrode. An Hg/HgO electrode (saturated KOH) was used as the reference, and a coiled Ni wire functioned as the counter electrode. The electrolyte consisted of 1 M KOH (Titripur, Merck), which was continuously saturated with oxygen during all measurements to maintain defined OER conditions. Prior to activity evaluation, samples were activated via cyclic voltammetry (CV). An initial series of 50 cycles was performed between 0.10 and 1.20 V_{RHE} at 20 mV s^{-1}, followed by 200 cycles in the range of 1.20–1.60 V_{RHE} at the same scan rate. Oxygen evolution reaction (OER) performance was evaluated using linear sweep voltammetry (LSV) recorded at 2 mV s^{-1} before and after cycling under OER conditions. All measurements were conducted using a Biologic SP-300 potentiostat with 85 % iR compensation applied.

To assess the electrochemical surface area of the samples, double-layer capacitance (C_{dl}) methodology was used. Cyclic voltammograms were recorded in Ar-saturated 1 M KOH at various scan rates between 500 and 10 mV s^{-1}. The C_{dl} was estimated by plotting the average of the anodic (j_a) and cathodic (j_c) current density against the scan rate, where the slope is C_{dl}. The average double layer capacitive current density (j_{avg}) is given by the equation $j_{avg} = (j_a + |j_c|)/2 = C_{dl} \times \nu$, where ν is the scan rate.

To evaluate long-term operational stability, a chronopotentiometric test at a constant current density of 10 mA cm^{-2} was performed for 24 h in O_2-saturated 1 M KOH using the same three-electrode configuration as described above. The potential was recorded continuously, and no additional iR correction was applied during the stability measurement.

The IrO_x benchmark catalyst (Premion, Alfa Aesar) was evaluated in a three-electrode setup. A thin film of IrO_x powder was deposited onto a glassy carbon rotating disk electrode (RDE), which served as the working electrode, while a HydroFlex reversible hydrogen electrode (Gaskatel GmbH) and a carbon rod were used as the reference and counter electrodes, respectively. The films were prepared by drop-casting 20 µL of an IrO_x ink, obtained by dispersing the nanoparticles in Milli-Q water (18.2 MΩ cm). A 5 % Nafion stock solution (Aldrich) was added so that Nafion represented 25 wt% of the total solids in the suspension. The electrochemical protocol consisted of 20 CV scans at 50 mV s^{-1} between 0.05 and 1.45 V, followed by activity assessment using an LSV from 1.2 to 1.6 V at 2 mV s^{-1}. Both activation and activity measurements were carried out in Ar-purged electrolyte, and the activity test was then repeated under O_2-saturated conditions.

***Mimicked in situ* Raman spectroelectrochemical measurements.** The Raman spectra were measured with the confocal Raman WITec spectrometer Alpha 300. The spectra were recorded with a 532 nm laser at a power of 1 mW, 20× objective, and an integration time of 1 s. 100 scans were acquired for each measurement. The measurements were performed for: a) the IN625-LT starting sample, which was subsequently treated electrochemically. First, ten CV cycles between 1.20 and 1.55 V_{RHE} were performed at a scan rate of 20 mV s^{-1} to activate the electrode surface. The scan rate was then reduced to 2 mV s^{-1}, and the measurement protocol involved pausing these slow scans at the following potentials: b) after the Ni oxidation peak at 1.45 V_{RHE} (close to the OER onset potential); c) at 1.55 V_{RHE} (anodic potential limit in the OER region); d) at 1.20 V_{RHE} (after the reduction peak of Ni^{3+}). After each electrochemical treatment (b-d), the *mimicked in situ* spectra were measured after the sample was transferred to the Raman spectrometer with a droplet of 1 M KOH electrolyte. The electrolyte droplet acted as a protective layer, preventing any possible rapid changes under atmospheric conditions.

2.3. Data management

The experimental data were systematically managed using the Qx application (Quipnex, Ljubljana, Slovenia). The software enabled structured documentation of all steps, including sample preparation, surface treatment, characterization, and electrochemical tests.

3. Results and discussion

3.1. Structural characteristics of the laser treated sample (IN625-LT)

To investigate the structural and compositional changes induced by the laser treatment, the pristine IN625 and laser-treated IN625-LT samples, as well the sample IN625-LT_EC_ST obtained after the electrochemical stability test, were characterized by XRD analysis (Fig. 1). The diffraction pattern of pristine IN625 exhibits the characteristic peaks of Inconel 625, and can be indexed as a single-phase, face-centered cubic (FCC) austenitic γ-(Ni,Cr,Fe) solid solution, strengthened by Mo and Nb, and containing only very small amounts of γ",δ, and carbide precipitates, which are usually below the detection limit of laboratory XRD in the as-processed state. Prominent reflections are observed at $2\theta \approx 43.4°$, 50.5°, 74.2°, 90.1°, and 95.3°, corresponding to the (111), (200), (220), (311), and (222) planes of the γ phase, respectively. This diffraction behavior is consistent with reports on conventionally processed and additively manufactured IN625 and is in very good agreement with previously published XRD patterns of IN625 produced by different processing routes [17,18,20–22].

The same set of γ-phase peaks, with unchanged positions and relative intensities, is observed for the laser-treated sample IN625-LT and remains essentially unchanged after electrochemical stability test (IN625-LT_EC_ST), confirming that the bulk of the alloy retains a γ-(Ni,Cr,Fe,Mo,Nb) solid-solution structure and that no additional crystalline secondary phases appear within the detection limit of XRD. This behavior is expected because the laser-modified or activated layer is only a few µm thick and consists mainly of 2–5 nm Ni-based hydroxide or nanooxide particles embedded in an amorphous matrix; such nanocrystalline or amorphous surface phases produce very broad and weak diffraction features that are largely overshadowed by the much stronger signal from the underlying metallic substrate, especially considering the 5–20 µm X-ray penetration depth for Cu Kα radiation.

To overcome the limitation of XRD bulk analysis, TEM microscopy was employed, where the sample was prepared by placing a droplet of deionized water on the laser-treated surface, gently scratching it with a

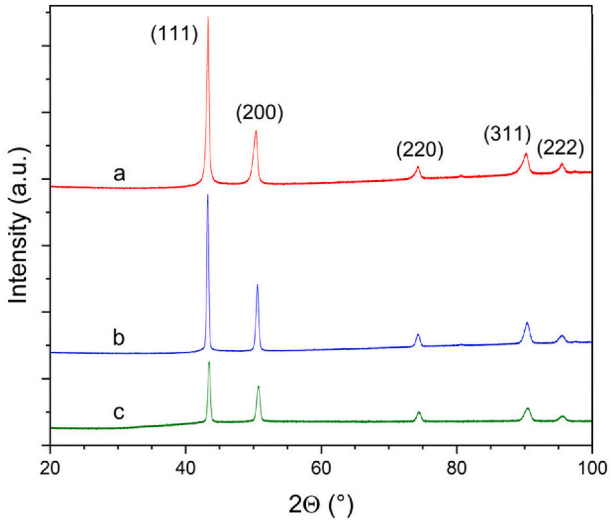

Fig. 1. XRD diffractograms of a) pristine IN625, b) IN625-LT and c) IN625-LT_EC_ST samples.

scalpel, and then immersing a TEM grid into the suspension. The TEM micrographs (Fig. 2A–C) show that 2–5 nm sized nanoparticles were formed during the laser treatment, and the FFT analysis confirms the onset of crystallization in these nanoparticles. The experimental SAED pattern shows broad and diffuse rings corresponding to the cubic NiO bunsenite phase (Fig. 2D). Although the SAED pattern is primarily indicative of the bunsenite phase, elemental EDXS mapping reveals a homogeneous distribution of all alloying elements at the submicrometer scale in the IN625-LT sample (Fig. 2E, Figs. S1 and S2, and Table S1 in *Supplementary Information (SI)*). This suggests that while NiO represents the predominant crystalline phase, other elements remain distributed throughout the laser-modified layer, likely in amorphous or poorly crystalline forms. The XRD and TEM findings are further supported by Raman spectroscopy, which confirms the presence of short-range ordering and poorly crystalline oxide layers on the surface of the IN625-LT (see section on Raman spectroscopy below).

The compositional changes induced by the laser treatment were quantified using SEM-EDXS analysis (Figs. S3 and S4, Table S2 in the *SI*). The pristine IN625 alloy exhibits a composition characteristic of Ni-based superalloy: Ni (61.8 at.%), Cr (23.6 at.%), Fe (6.9 at.%), Mo (5.2 at.%), and Nb (2.1 at.%), with minimal oxygen content (0.4 at.%). After laser treatment (IN625-LT), substantial surface oxidation occurs, as evidenced by an increase in oxygen content to 42.5 at.%. This oxidation is accompanied by a proportional decrease of all metallic elements: Ni (37.1 at.%), Cr (12.1 at.%), Fe (4.1 at.%), Mo (3.0 at.%), and Nb (1.2 at.%). However, the ratios of the at.% concentrations of the different elements relative to Ni show an unchanged stoichiometry (the ratios of Fe/Ni, Mo/Ni, Nb/Ni remain constant), while only the ratio of Cr/Ni exhibits a slight decrease (~13 %). This indicates a preferential loss of Cr from the surface during the high-temperature laser treatment, although it was performed in the presence of considerable amounts of Ar. This redistribution of elements is confirmed by EDXS mapping, which shows the spatial distribution of each element on the laser-treated IN625-LT surface (Fig. S4 in the *SI*).

Surface morphology analysis of the untreated Inconel 625 alloy (Fig. 3A, E) shows a smooth metallic surface with well-defined grain boundaries and no nanoscale structuring. This morphology is characteristic of Ni-based superalloys and provides a low electrochemically active surface area, consistent with the poor OER performance observed for the untreated sample. Laser treatment induces a profound transformation of the surface (Fig. 3B, F). IL-SEM imaging reveals the formation of uniformly distributed hierarchical nanostructures across the entire treated region. These structures can be categorized into three characteristic regions marked in Fig. 3B: spherical domains (red), elongated interconnected structures (yellow), and ridge-like interconnected zones (orange). Higher magnification imaging of the spherical domains (Fig. 3F) reveals a distinct 'cauliflower-like' substructure consisting of fine features, confirming the large surface area architecture

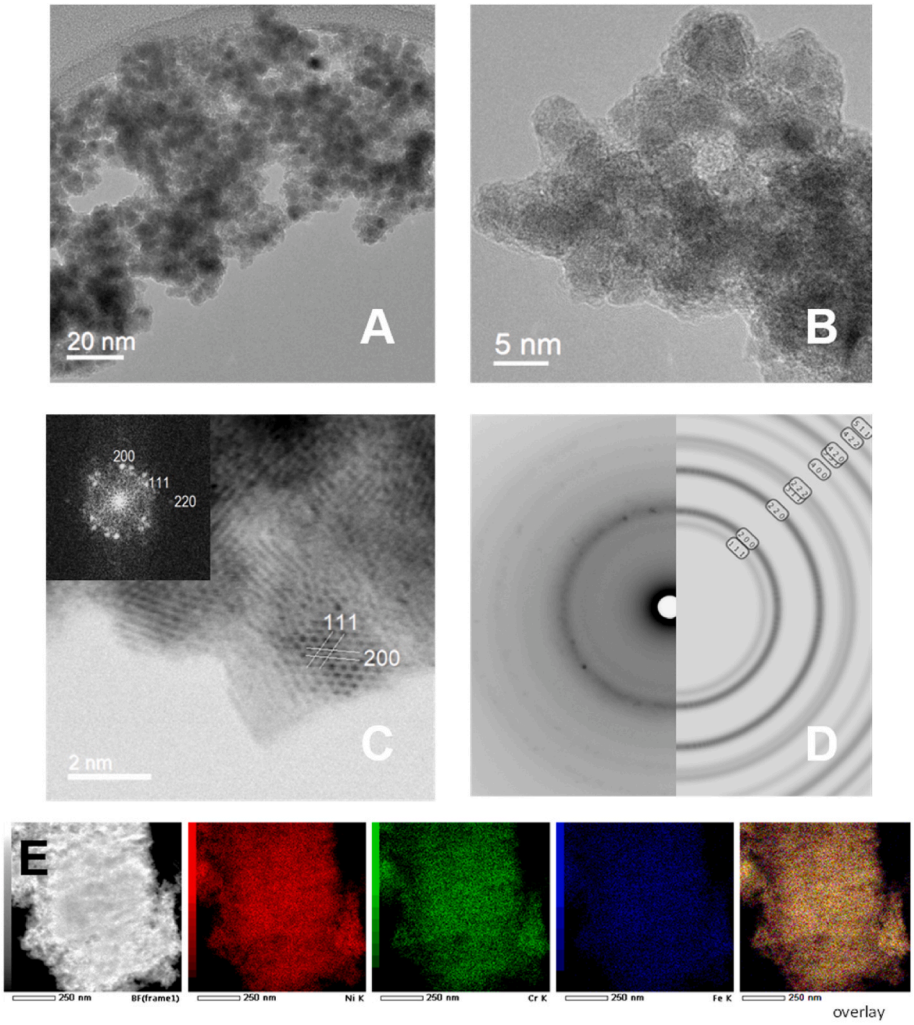

Fig. 2. A,B) TEM micrographs of the IN625-LT sample at different magnifications. C) The BF/STEM micrograph of 2–5 nm sized nanoparticles with labelled crystal planes. The inset shows the indexed FFT of the micrograph indicating poorly crystallized particles. D) Experimental SAED (left) and simulated diffraction pattern (right) for cubic NiO (bunsenite). E) Elemental EDXS mapping with the main Ni, Cr, Fe elements shown.

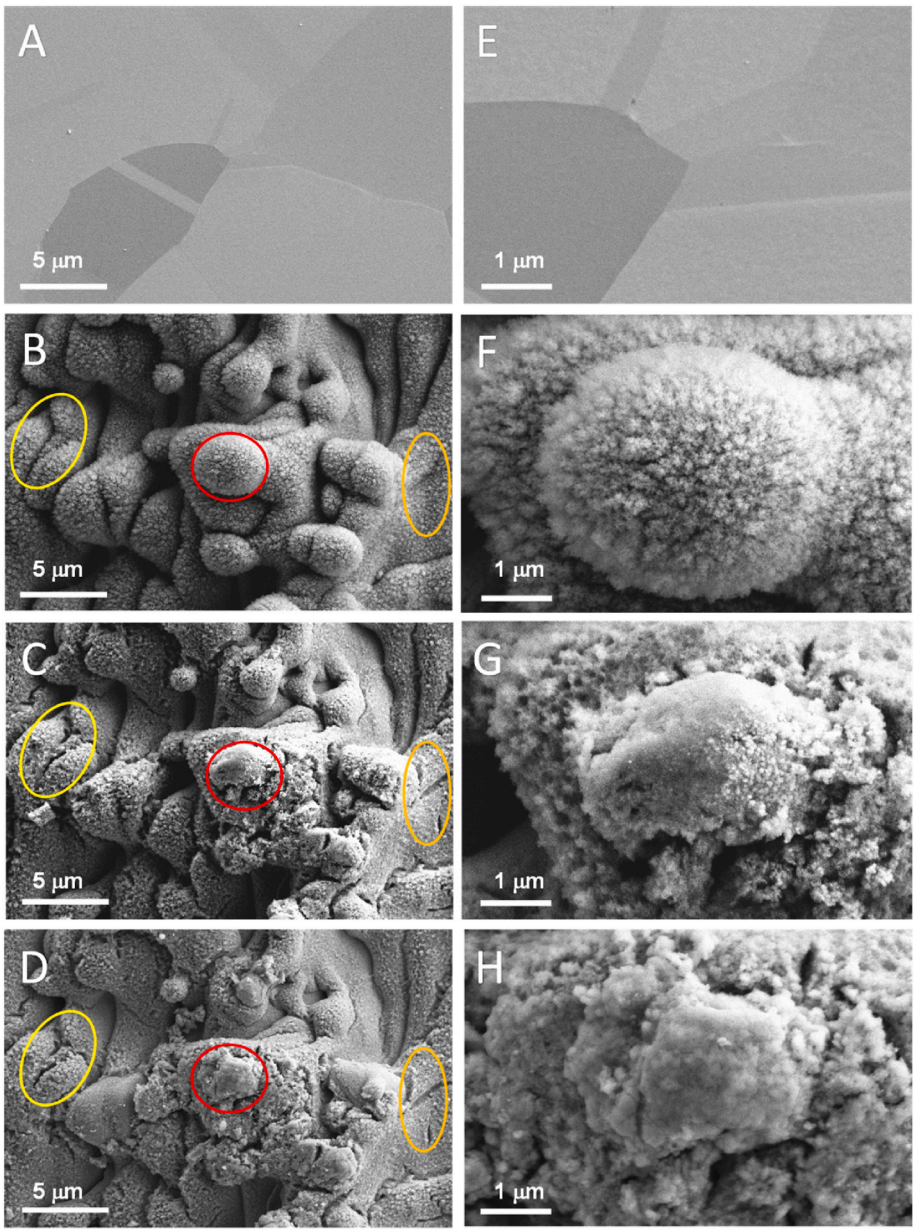

Fig. 3. SEM images of: A,E) untreated IN625 surface, B,F) the laser-treated IN625-LT surface, C,G) the electrochemically treated IN625-LT_EC surface, and D,H) the surface after the 24 h stability test at 10 mA cm^{-2}. B,C,D) Low magnification SEM images highlighting three characteristic surface areas - spherical domains (red), elongated interconnected structures (yellow), and ridge-like interconnected zones (orange). F,G,H) Higher-magnification images of the area of spherical domains before and after electrochemical treatment. Progressive changes in surface morphology, including partial coalescence, smoothing of nanoscale features, and localized cracking, are observed after electrochemical cycling and long-term operation. These transformations are consistent with the selective dissolution of Cr and Mo. (For interpretation of the references to colour in this figure legend, the reader is referred to the Web version of this article.)

observed in the TEM analysis (Fig. 2).

After electrochemical treatment (Fig. 3C, G), pronounced morphological changes are observed on the IN625-LT_EC surface. The originally continuous nanostructures partially coalesce and locally flatten, accompanied by the appearance of fine cracks and voids between adjacent domains. These features indicate localized dissolution and restructuring of the oxide layer during OER cycling. The smoothing of the characteristic "cauliflower-like'' features is consistent with the selective dissolution of Mo and Cr detected by SEM-EDXS analysis.

After the 24 h stability test (Fig. 3D, H), the surface shows further morphological evolution relative to the electrochemically activated state. The hierarchical structures remain recognizable, but the nanoscale features become progressively less defined. The spherical domains appear more compacted and irregular, with partial collapse of their characteristic "cauliflower-like" texture. These changes are consistent with the continued loss of less stable alloying elements during long-term OER operation, which leads to gradual smoothing and restructuring of the surface. Despite this evolution, the overall high-surface-area architecture remains present.

3.2. *Electrochemical surface evolution and OER performance*

Electrochemical activation of the laser-treated IN625-LT surface in 1 M KOH led to pronounced compositional and morphological transformations, accompanied by a substantial enhancement in OER performance (Fig. 4). Post-activation SEM-EDXS analysis revealed a marked increase in oxygen content (from 42.5 to 60.4 at.%) and a corresponding decrease in Ni (to 29.7 at.%), with Cr falling below the detection limit,

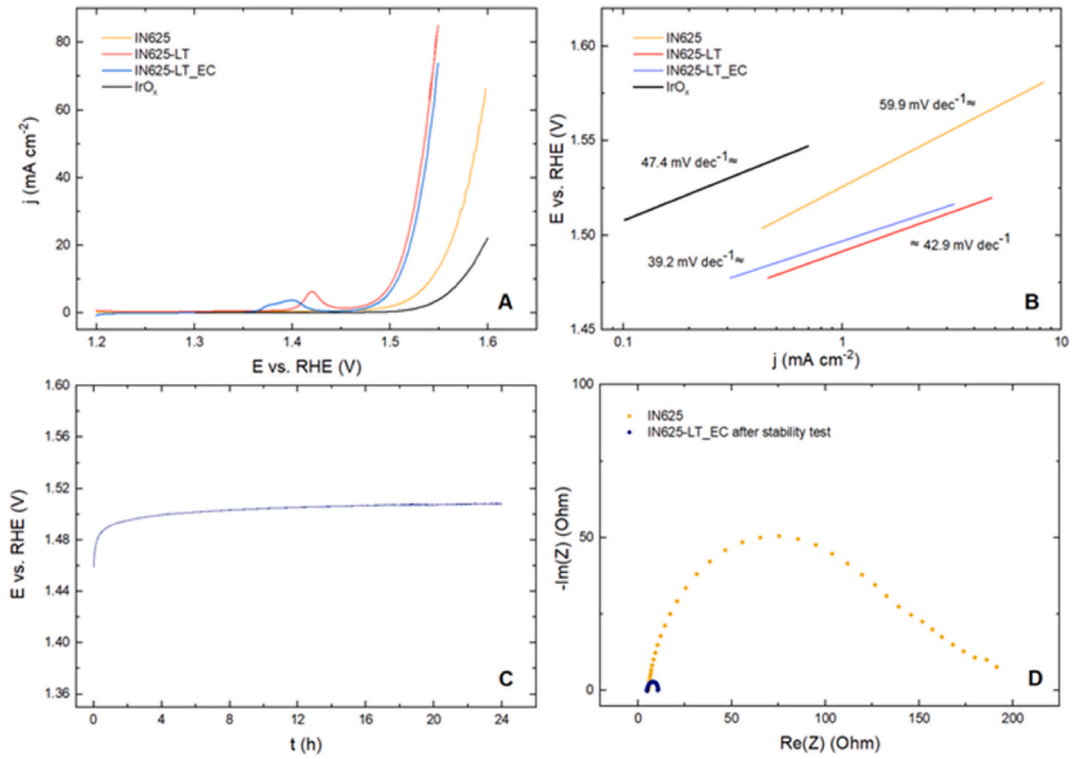

Fig. 4. OER activity and stability of laser-treated Inconel 625. A) Polarization curves showing significantly enhanced OER performance of laser-treated samples (IN625-LT and IN625-LT_EC) compared to pristine IN625 and IrO_x benchmark. B) Tafel analysis demonstrating improved OER kinetics, with Tafel slopes decreasing from 59.9 mV dec^{-1} (pristine IN625) to 39.2 mV dec^{-1} (IN625-LT_EC). The measurements were recorded in oxygen-saturated 1 M KOH at a scan rate of 2 mV s^{-1}. C) Chronopotentiometric stability measurement at 10 mA cm^{-2} for 24 h showing only a slight increase in potential, confirming stable long-term operation. D) Electrochemical impedance spectra (Nyquist plots) recorded at 1.50 V_{RHE} for the pristine alloy and after the 24 h stability test, demonstrating a substantial decrease in charge-transfer resistance after surface reconstruction.

consistent with its rapid dissolution under alkaline conditions [23]. Mo was also significantly depleted, Nb slightly, while Fe content increased from 4.1 to 7.9 at.%, indicating Fe incorporation from both the alloy matrix and the electrolyte. These changes point to progressive oxidation, selective removal of less stable alloying elements, and restructuring of the oxide layer during electrochemical cycling. The impact of these transformations on Ni^{2+}/Ni^{3+} redox behavior and OER activity is discussed below.

Ni^{2+}/Ni^{3+} oxidation. A characteristic feature of activated Ni-based electrocatalysts is the appearance of a Ni^{2+}/Ni^{3+} oxidation peak that precedes oxygen evolution. For the IN625-LT sample, this peak appears at approximately 1.42 V_{RHE} (Fig. 4A), which is consistent with literature values for the conversion of $Ni(OH)_2$ to Ni^{3+}-oxyhydroxide phase [3–6, 24–28]. The potential of Ni^{2+}/Ni^{3+} oxidation varies in the literature, in part due to different preparation routes, substrates, and electrochemical activation procedures, but several basic principles can be established. The potential of α-$Ni(OH)_2$/γ-NiOOH depends on the nature of these phases, which are characterized by intercalated water molecules and anions between the layers. When β-$Ni(OH)_2$/β-NiOOH structures are formed by electrochemical cycling or aging in alkaline media, the potential shifts to a more positive potential [5,6]. Similarly, the incorporation of Fe into Ni-based samples shifts the oxidation potential in the anodic direction [5,6]. The IN625-LT_EC sample shows a particularly interesting behavior, exhibiting overlapping oxidation peaks: the main peak at 1.40 V_{RHE} and a shoulder at ~1.38 V_{RHE}. Evidently, the shift of the IN625-LT peak at 1.42 V_{RHE} to more negative potentials and its splitting (IN625-LT_EC) confirm the gradual transformation and hydration of the originally amorphous oxide surface (Fig. 4A). The peak splitting for the IN625-LT_EC sample suggests the formation of more hydrated α-$Ni(OH)_2$/γ-NiOOH phases, possibly also a γ-NiOOH phase with incorporated Fe [5,6]. Cr and Mo are unlikely to contribute to these peaks, as SEM-EDXS analysis (Figs. S3 and S4 in the *SI*) shows that they dissolve almost completely from the IN625-LT-EC surface. Niobium, which is only present in minor quantities, typically oxidizes at lower potentials than the range we investigated [29]. Therefore, the observed peak splitting most likely originates from different Ni-based phases.

In contrast, the pristine IN625 surface shows no Ni or Cr oxidation peaks in the potential range up to around 1.50 V_{RHE}, where oxygen evolution starts (Fig. 4A). This behavior confirms the high electrochemical stability of Inconel 625 and is consistent with reports of stainless steels containing Cr and Ni in alkaline media [30].

OER activity. The laser treatment significantly enhanced OER performance. The pristine IN625 sample (Fig. 4A) shows oxygen evolution onset above 1.50 V_{RHE}, i.e. the onset potential being defined as the potential where the anodic current exceeds 0.1 mA cm^{-2} above the non-faradaic baseline. The potential required to achieve 10 mA cm^{-2} is 1.55 V_{RHE}, corresponding to an overpotential (η_{10}) of 320 mV. In contrast, the laser-treated IN625-LT sample exhibits an onset potential of approximately 1.47 V_{RHE}, with the current density increasing to approximately 85 mA cm^{-2} at 1.55 V_{RHE}. The potential required to reach 10 mA cm^{-2} decreases to 1.50 V_{RHE}, giving $\eta_{10} = 270$ mV. After electrochemical treatment (IN625-LT_EC), the onset potential shifts slightly to positive, resulting in 73 mA cm^{-2} at 1.55 V_{RHE}. The potential required to achieve 10 mA cm^{-2} is 1.51 V_{RHE}, giving $\eta_{10} = 270$ mV, which is 74 mV lower than the one of the IrO_x benchmark with an overpotential of 344 mV.

The electrochemically active surface area was assessed through double-layer capacitance (C_{dl}) measurements (Fig. S7). The pristine IN625 surface exhibited a C_{dl} of 98 μF cm^{-2}, while laser treatment significantly increased the C_{dl} to 456 μF cm^{-2} for IN625-LT. When the current densities are normalized by their respective C_{dl} values to account for the differences in surface area, the laser-treated sample demonstrates

1.5 times higher intrinsic activity per electrochemically active area compared to pristine IN625. This indicates that the enhanced OER performance arises from both increased surface area (4.7 times higher) and improved catalytic efficiency per active site, likely due to surface restructuring and Cr depletion that creates more favorable active sites for OER.

In the OER region, the measured data in Fig. 4A align with previous reports. The OER activity of pure $Ni(OH)_2$ is generally relatively low, whereas the incorporation of Fe significantly enhances its performance and shifts the onset of OER to more cathodic potentials [5,6,26]. The surface modifications induced by the laser treatment allow Fe to be incorporated from both - the alloy matrix and the electrolyte - into the Ni $(OH)_2$ formed on the surface, thereby positively influencing the OER activity.

Tafel slope analysis confirms the enhanced OER kinetics of the laser-treated surfaces (Fig. 4B). The pristine IN625 exhibits sluggish kinetics with a Tafel slope of 59.9 mV dec^{-1}, while the laser treatment improves the value to 42.9 mV dec^{-1} for IN625-LT. Electrochemical treatment further enhances the kinetics, yielding a Tafel slope of 39.2 mV dec^{-1} for IN625-LT_EC, whereas the one for the IrO_x benchmark was 47 mV dec^{-1}. These values align well with literature reports for Ni-based and mixed Ni/Fe electrocatalysts. For comparison, Louie et al. [6] reported approximately 55 mV dec^{-1} for Ni-based films and approximately 40 mV dec^{-1} for mixed Ni/Fe-based films, while Fukushima et al. [4] determined 62 mV dec^{-1} for Ni-based nanohole-array electrodes. The systematic improvement of the Tafel slopes correlates with the structural and compositional evolution of the surface: the removal of Cr/Mo-containing passive film and creation of the hierarchical nanostructure by the laser treatment. This provides increased surface area for formation of highly active Ni-rich and Fe-incorporated α-Ni $(OH)_2$/γ-NiOOH layer, that facilitates charge transfer and O–O bond formation on Ni–Fe sites dominating the kinetics and yielding the characteristic ~40 mV dec^{-1} slope of highly active OER catalysts. EDXS analysis quantifies this Fe incorporation, showing increased Fe/Ni atomic ratio from 0.11 (IN625-LT) to 0.27 (IN625-LT_EC), confirming substantial Fe uptake during electrochemical cycling.

Long-term stability and electrochemical impedance spectroscopy. The long-term operational stability of the catalyst was evaluated using a 24 h chronopotentiometric test at a constant current density of 10 mA cm^{-2} (Fig. 4C). Throughout the measurement, the potential remained essentially stable, fluctuating only within a narrow range due to bubble formation at the electrode surface, indicating no measurable degradation of catalytic activity.

To further probe the charge-transfer characteristics, electrochemical impedance spectroscopy was performed at 1.50 V_{RHE} for the pristine alloy and for the sample after the 24 h stability test (Fig. 4D). The untreated IN625 exhibits a large semicircle characteristic of slow charge-transfer kinetics, whereas the post-stability surface shows a markedly reduced semicircle, consistent with the formation of a conductive and catalytically active Ni-rich oxyhydroxide layer. These Nyquist plots corroborate the improved kinetics observed in the Tafel analysis and confirm that the catalyst maintains low charge-transfer resistance after extended operation.

3.3. Chemical state analysis

XPS analysis confirmed the findings explained above. For the starting IN625-LT sample, the O 1s spectrum (Fig. 5A) exhibits a main peak at 529.9 eV, originating from metal oxides. A high binding energy shoulder at approximately 531.0 eV indicates that some metal hydroxides have already formed at the surface [31]. After electrochemistry, the main O 1s peak shifts to 531.0 eV, suggesting an enrichment of metal hydroxides on the surface of the IN625-LT_EC sample. The Fe 2p spectra (Fig. 5B) show pronounced noise due to the low Fe surface concentration. Interpretation is further hindered by the overlap with the Ni LMM Auger feature, which complicates Fe 2p spectra interpretation. For both

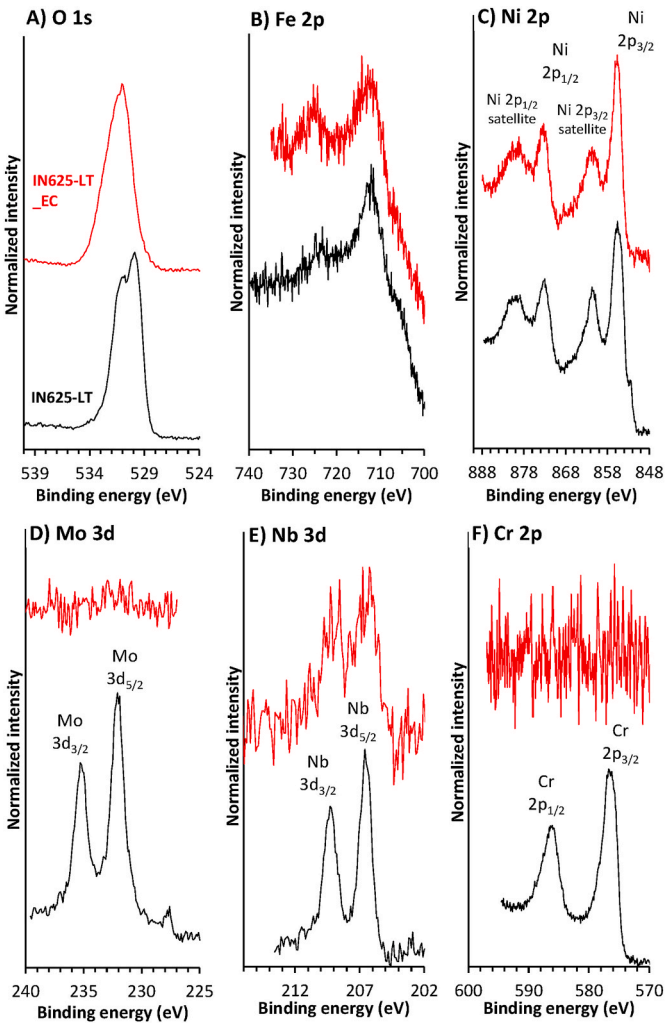

Fig. 5. High-resolution XPS spectra for the laser-treated IN625-LT sample (lower black spectra) and sample IN625-LT_EC after electrochemical treatment (upper red spectra): A) O 1s, B) Fe 2p, C) Ni 2p, D) Mo 3d, E) Nb 3d, and F) Cr 2p. (For interpretation of the references to colour in this figure legend, the reader is referred to the Web version of this article.)

samples, IN625-LT and IN625-LT_EC, the Ni $2p_{3/2}$ peak appears at 855.6 eV, accompanied by the characteristic shake-up satellite structure (Fig. 5C). As the Ni 2p XPS spectra are similar for $Ni(OH)_2$ and NiOOH phases [31], one of these species or both might be present at the surface. For the IN625-LT sample, the intense satellite at ~861–862 eV is also consistent with a Ni^{2+} hydroxide environment. Although NiOOH (Ni^{3+}) also exhibits a main $2p_3/_2$ peak near 855.5–856.0 eV, the differentiation between $Ni(OH)_2$ (Ni^{2+}) and NiOOH (Ni^{3+}) is challenging by XPS alone because: their $2p_3/_2$ binding energies overlap, both phases exhibit similar shake-up satellite structure, the Ni 2p region suffers from multiplet splitting and broadening, making precise assignments difficult [32]. Narrowing of the Ni 2p peak has been reported during the transformation of mixed Ni^{2+}/Ni^{3+} oxyhydroxides toward more hydroxide-rich surfaces. Therefore, the spectra are more consistent with dominant Ni^{2+} ($Ni(OH)_2$) rather than significant Ni^{3+} (NiOOH) formation. The absence of additional satellite suppression or the slight +0.3–0.5 eV shift typically associated with NiOOH also supports this conclusion. Thus, while Ni^{3+}-containing species cannot be fully excluded, the spectra primarily indicate the presence of Ni^{2+} hydroxide, which becomes more prevalent after electrochemical treatment.

After electrochemical treatment, Cr- and Mo-related species were no longer detected by XPS (Fig. 5D, F), which confirms their removal from

the surface of the IN625-LT_EC sample, as has also been shown by EDXS (Figs. S3 and S4, and Table S2 in the *SI*). For the same sample, the Nb signal (Fig. 5E) remained non-intense, indicating its low surface atomic concentration. ToF-SIMS analysis confirmed the presence of Nb-containing species after electrochemistry (Fig. 6). It must be pointed out that ToF-SIMS has a lower detection limit than XPS. Moreover, using ToF-SIMS, a depth profiling was performed, while an XPS experiment was performed without sputtering. Cr- and Mo-related signals were not detected by ToF-SIMS, implying their effective dissolution from the outermost surface layers after electrochemical treatment. Before electrochemical treatment, both Mo 3d and Cr 2p peaks were measured, confirming that Mo and Cr were initially present on the surface (Mo $3d_{5/2}$ at 232.0 eV and Cr $2p_{3/2}$ at 576.3 eV, Fig. 5D, F).

In ToF-SIMS, the M^- (where M represents metal) signal indicates metallic elements and/or their oxidized forms on the surface (M^- can originate from metal and metal oxide/hydroxide/oxyhydroxide). The MO^- and MOH^- ions result from oxygen-bound metal species and are characteristic of metal oxides/hydroxides/oxyhydroxides [33–35]. The 3D ToF-SIMS reconstruction shown in Fig. 6 presents the spatial distributions of Fe, Ni, and Nb-related signals. The Ni-related species dominate the surface, appearing across the analyzed area, consistent with the XPS results indicating the presence of $Ni(OH)_2$ (Fig. 5C). Notably, the metallic Ni^- signal extends throughout the entire analyzed depth, whereas the oxidized NiO^- and $NiOH^-$ species are strongly enriched in the uppermost surface region, reflecting the formation of a thin Ni-based oxide/oxyhydroxide layer on the electrochemically conditioned alloy. Fe-related signals are detected to a lesser extent, with localized regions of higher intensity suggesting surface heterogeneity or partial enrichment. The presence of FeO^- and $FeOH^-$ signals indicates that Fe is present predominantly in oxidized states, not in metallic form. Moreover, the Nb-related signals are confined to discrete domains or subsurface regions. This agrees with SEM-EDXS results showing that Nb is partially dissolved during electrochemical cycling.

Electrolyte analysis by ICP-OES provided additional evidence for selective element dissolution during electrochemical treatment. Analysis of the 1 M KOH electrolyte after the electrochemical treatment revealed dissolved Mo (0.25 mg L^{-1}) and Fe (0.09 mg L^{-1}), while Ni remained below detection limits (<1 mg L^{-1}). This confirms the preferential leaching of Mo observed by the analyses presented above and indicates that Fe dissolution occurs alongside the formation of Fe-incorporated Ni-based phases. Note that Cr and Nb were not included in the ICP-OES analysis. However, the dissolution of Cr is clearly evidenced by its complete absence from post-cycling EDXS and XPS data (Fig. 5, Figs. S3 and S4, and Table S2 in the *SI*).

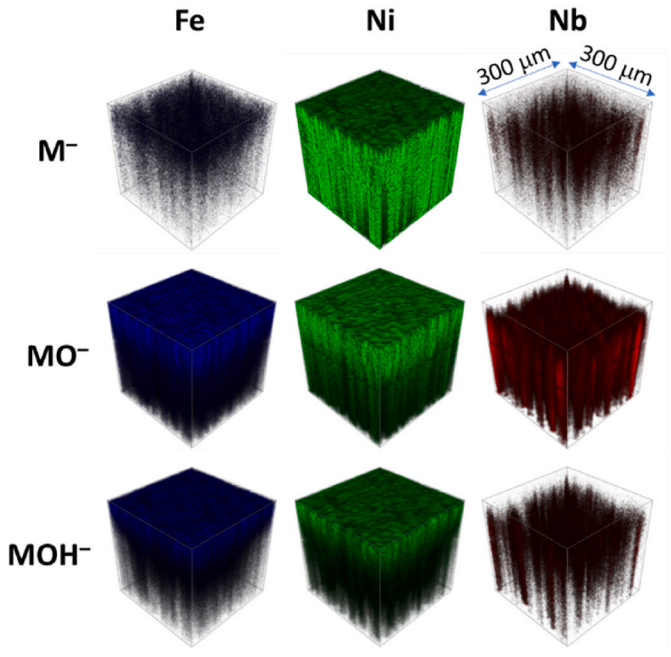

Fig. 6. 3D ToF-SIMS images of IN625-LT_EC showing the spatial distribution of Fe, Ni, and Nb-related species.

3.4. *Mimicked in situ* Raman spectroelectrochemistry

Mimicked in situ Raman spectroelectrochemistry was performed to corroborate the phase transformations in the IN625-LT sample. Since NiOOH phase exhibits characteristic Raman spectrum, the measurements were extended to the potential region of Ni^{3+} formation. Raman spectra were recorded at four key potentials: a) the starting IN625-LT sample, b) after the oxidation peak to Ni^{3+} at 1.45 V_{RHE} (near the onset of OER), c) in the OER region (1.55 V_{RHE}), and d) after reduction to Ni^{2+} (1.20 V_{RHE}). To minimize atmospheric effects and preserve the electrochemical state, the samples were transferred to the spectrometer with a droplet of electrolyte remaining on the surface. The *mimicked in situ* Raman spectra are presented in the spectral range of 200–3700 cm^{-1} (Fig. 7), also showing the characteristic bands of electrolyte water (bending mode at 1650 cm^{-1} and a broad band between 3000 and 3700 cm^{-1}). Enlarged spectral regions of the same spectra are provided in Fig. S5 (SI).

The Raman spectrum of the IN625-LT sample (Fig. 7a) shows several overlapping broad, low-intensity bands, which are characteristic of heterogeneous mixtures of metal oxides, possibly also hydroxides, in amorphous or poorly crystalline form (Fig. 1). The broad shoulder band between 480 and 530 cm^{-1} can be associated with the Ni–O or Ni–OH stretching vibrations [36,37]. Additional features are consistent with the amorphous/poorly crystalline oxide/hydroxide phases of other alloying elements, i.e. Cr (550–600 cm^{-1}) [30,38], Fe (around 500 cm^{-1} and 600–700 cm^{-1}) [6,39], and at around 700–850 cm^{-1} Mo [40] and Nb [41].

Formation of γ-NiOOH during oxidation. The spectrum measured at 1.45 V_{RHE} after oxidation peak (Fig. 7b) shows characteristic Ni^{3+}-containing species of NiOOH [3,28,37]. Two prominent bands appear at

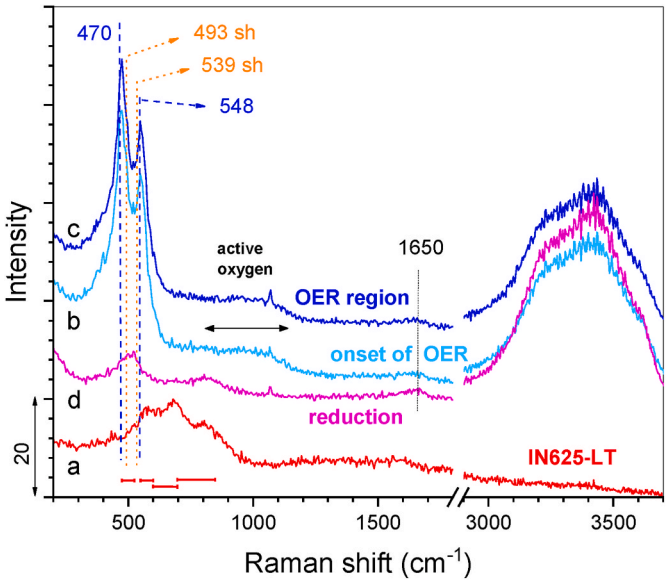

Fig. 7. *Mimicked in situ* Raman spectra of IN625-LT sample in the spectral range 200–3700 cm^{-1}: a) IN625-LT starting sample, b) after the oxidation peak to Ni^{3+} at 1.45 V_{RHE} (onset of OER), c) in the OER region at 1.55 V_{RHE}, and d) after reduction to Ni^{2+} (1.20 V_{RHE}). For the *mimicked in situ* Raman spectra measurements, the samples were transferred under the objective of the spectrometer with an electrolyte droplet. The broad band between 3000 and 3700 cm^{-1} is due to aqueous 1 M KOH electrolyte.

470 and 548 cm^{-1}, which correspond to the bending and stretching vibrations of Ni–O in γ-NiOOH. These positions are slightly lower than the typical literature values (474–482 cm^{-1} and 554–562 cm^{-1}) [3,5,6,24,37], indicating a more loose, structurally distorted, and weakly bound form of γ-NiOOH. The significantly enhanced intensity of these two bands compared to the bands of the starting IN625-LT sample (Fig. 7a) reflects the well-known resonance Raman enhancement of NiOOH [3,6,24].

OER region. The spectrum obtained in the OER region at 1.55 V_{RHE} (Fig. 7c) retains the main γ-NiOOH bands at 470 and 548 cm^{-1} (Fig. 7b) but also shows shoulders at 493 and 539 cm^{-1}. Although such features could, in principle, arise from structural disorder or the formation of a secondary oxyhydroxide phase, their appearance can also be attributed to Fe incorporation into the Ni-oxyhydroxide lattice. This process is well documented to enhance OER activity and induce characteristic spectral shifts in Ni-based electrocatalysts [42]. Numerous studies have demonstrated that Fe impurities from alkaline electrolytes readily incorporate into Ni-based matrices, thereby increasing OER activity [3,5,43]. For instance, Raman spectra of α-$Ni(OH)_2$/γ-NiOOH recorded in Fe-containing KOH electrolytes exhibited slower ageing to the β-$Ni(OH)_2$/β-NiOOH counterpart compared to Fe-free conditions [5]. With regard to Raman spectra, Klaus et al. [5] reported a red shift of the higher-frequency γ-NiOOH band from 560 cm^{-1} in Fe-free electrolyte to a lower value of 558 cm^{-1} in Fe-containing electrolyte. Similar small shifts of this band to lower wavenumbers were also observed by Garcia et al. [25] and Jing et al. [27]. Moreover, the study of Ni–Fe samples by Louie et al. [6] revealed (in addition to the red shift of the higher-frequency component) the convergence of the γ-NiOOH bands from 474 and 554 cm^{-1} in Fe-free Ni sample to 476 and 548 cm^{-1} in Ni–Fe(51 %) samples. Simultaneously, the authors [6] reported a significant decrease in the intensity ratio of these two bands (I(474)/I(554)), with increase of Fe content. In our case, Fig. 7b,c (and Fig. 5S A in the *SI*) shows a similar red shift and convergence of the γ-NiOOH bands - from 470, 548 cm^{-1} bands to shoulder positions at 493, 539 cm^{-1}. The intensity ratio I(470)/I(548) reaches 1.3, while it decreases to 1.1 for the shoulder pair I(493)/I(539). Accordingly, the incorporation of Fe into γ-NiOOH remains highly probable for our sample, as these shoulder features emerge exclusively under OER conditions and coincide with compositional changes observed by SEM-EDXS – namely, significant Cr and Mo depletion accompanied by Fe enrichment.

***Spectral region* 800–1150 cm^{-1}.** Under OER conditions, broad but very low-intensity Raman bands are observed between 800 and 1150 cm^{-1} in our spectra (Fig. 7; Figure S5 B, *SI*). These bands are detected both at the onset of OER (1.45 V_{RHE}) and within the OER region (1.55 V_{RHE}). We also verified their appearance at different locations on the sample, and they consistently remain present (Fig. S6, *SI*). In the literature, bands in the 800–1150 cm^{-1} region have been attributed to so-called 'active oxygen' species in NiOOH [3,4,25], as well as in Ni/Fe-oxihydroxides [26,43]. The term is not used consistently throughout the literature but can denote negatively charged $NiOO^-$ species at the surface (lattice oxygen), as well as can be attributed to superoxide groups (-OO), peroxide groups (-OOH) or oxygen atoms (O) [44]. Jiang et al. [26] assigned similar features on metal foils to negatively charged superoxides ($–OO^-$) on Ni, Co, Cu, and Ag (850–1200 cm^{-1}) and to peroxyl groups (–OOH) on Au (500–900 cm^{-1}). Different authors [3,44] confirmed the oxygen related nature of these bands by isotopic labelling of the electrolyte water ($H_2^{16}O$). Due to the possibility that various oxygen species are simultaneously existing on Ni and Ni/Fe surfaces, the 'active oxygen' bands are typically broad [4]. Trześniewski et al. [43] further reported that the signal intensity of these species does not necessarily increase with potential, but rather emerges already during Ni oxidation and remain present during OER. In line with these observations, our spectra measured at the onset of OER and within the OER region (Fig. 7; Figure S5 B, *SI*) show similar intensity of the 800–1150 cm^{-1} bands, suggesting that their intensity is rather related to the available surface than to the applied potential. The persistence of the 'active oxygen' bands in our spectra – even under *mimicked in situ* conditions – was unexpected, but it is in fact consistent with known behavior of $Ni(OH)_2$/NiOOH films. Such films have been extensively investigated as electrochromic films, where long-lived 'memory effects' – also for many hours – are attributed to the slow reduction of Ni^{3+} species and associated oxygen-based intermediates for extended periods even without applied potential or in atmosphere [45]. A controlled Raman experiment was also performed for DC magnetron sputtered films, following the reduction of NiOOH to $Ni(OH)_2$ with time in KOH electrolyte (at OCP), air and vacuum [46]. The films remained the bands of NiOOH in Raman spectra for up to 2 h if they were activated with cycling prior measurements. According to our experience in electrochromic films we would like to state that the reduction of NiOOH is much faster for highly porous films and nanoparticles than is for dense and covalently bonded films. Accordingly, the existence of short-living intermediates in our *mimicked in situ* spectra is not expected, but the presence of 800–1150 cm^{-1} bands suggests the presence of surface Ni-OO^- groups that can be stabilized by the presence of cations [25].

Reduction behavior. Upon reduction from Ni^{3+} to Ni^{2+} (Fig. 7d, Fig. S5 A, *SI*), the 'active oxygen' bands disappear and the overall spectral intensity decreases markedly. The most prominent change is the shift of the first band from 580 cm^{-1} in the starting IN625-LT (Fig. 7a and Figure S5 Aa) to a broad and intense band between 420 and 560 cm^{-1} (Fig. 7d and Figure S5 A d). This shift indicates the transformation of a large part of the sample, even in the bulk, to Ni-hydroxide and Fe/Ni-hydroxide during cycling and the appearance of Ni^{2+}-OH vibrations. The other two bands at 681 cm^{-1} (very low intensity) and 802 cm^{-1} (Fig. 7d) reappear at the positions of the IN625-LT starting sample (Fig. 7a) but have much lower intensity, consistent with partial depletion of Cr and Mo and possible modification of Ni-based structures by Fe incorporation.

3.5. Integrated discussion of surface transformation mechanism

The comprehensive characterization reveals a complex surface evolution process that explains the enhanced electrocatalytic performance of the laser-treated Inconel 625. Initially, the laser treatment creates hierarchical nanostructures consisting mainly of amorphous/poorly crystalline phases while maintaining the homogeneous distribution of all alloying elements (EDXS mapping). The presence of 2–5 nm sized NiO nanoparticles was found by TEM while XPS shows the predominance of $Ni(OH)_2$ at the surface. The nanostructuring significantly increases the electrochemically active surface area, as evidenced by C_{dl} measurements.

During electrochemical activation, selective dissolution occurs with complete removal of Cr and a considerable depletion of Mo (EDXS, XPS, ToF-SIMS, ICP-OES), leaving behind a Ni-rich surface. Crucially, it seems that Fe could be incorporated into the developing $Ni(OH)_2$ structure from both the alloy matrix and the electrolyte. Raman spectroscopy suggests the formation of two catalytically active γ-NiOOH phases. The first γ-NiOOH phase is evident from the appearance of intense bands at 470 and 548 cm^{-1} while the shoulders at 493 and 539 cm^{-1} indicate another γ-NiOOH phase, presumably the phase with incorporated Fe.

The enhanced OER mechanism involves synergistic Ni–Fe interactions within the oxyhydroxide structure, supported by: (1) the appearance of low-intensity bands between 800 and 1150 cm^{-1} in Raman during OER conditions, (2) improved Tafel slopes (59.9 → 39.2 mV dec^{-1}), and (3) cathodic shift of the onset potential (~30 mV). The hierarchical nanostructure facilitates mass transport and bubble release, while the Ni–Fe oxyhydroxide provides intrinsic catalytic activity.

Stability mechanisms include the strong adhesion between the oxide layer and metallic substrate (formed through high-temperature laser fusion) and the elimination of less stable alloying elements that could cause degradation.

At this point we would also like to stress that Inconel 625 was

intentionally chosen for our experiments due to its industrial relevance and compositional complexity. We firmly believe that Ni–Fe alloys or even pure Ni metal under Fe-containing alkaline conditions would yield comparable Fe-incorporated γ-NiOOH active phases. The herein reported results thus not only illustrate the catalytic conversion of an industrially important alloy but also offer a framework applicable to Ni- and NiFe-based systems.

4. Conclusion

This study demonstrates that pulsed laser surface engineering represents an effective approach for transforming commercial Inconel 625 alloy into an active OER electrocatalyst. The single-step laser treatment creates hierarchical nanostructures that improve both surface area and catalytic activity, resulting in a 30 mV cathodic shift in OER onset potential and improved Tafel slope from 59.9 to 39.2 mV dec^{-1}.

The main advantages of this approach include: (1) direct conversion of an industrially available, mechanically robust substrate into a functional electrocatalyst without additional binders or complex synthesis steps, (2) formation of stable Ni-based and Ni–Fe-based oxyhydroxide active phases, through selective element dissolution and Fe incorporation into the Ni-matrix, and (3) good electrochemical durability due to the strong adhesion between the catalytic layer and the substrate, with the Ni-based framework retaining its activity despite possible phase transitions during cycling.

Raman spectroscopy provides crucial mechanistic insights: confirms the formation of two catalytically active γ-NiOOH phases and the presence of low-intensity bands between 800 and 1150 cm^{-1} under OER conditions. While 470 and 548 cm^{-1} bands belong to γ-NiOOH phase, the shoulders at 493 and 539 cm^{-1} are suggested to reflect the Fe incorporation into γ-NiOOH. The reversible appearance and disappearance of these spectral features demonstrates the electrochemically driven nature of active phase formation.

Beyond the specific material studied, this work establishes laser surface engineering as a promising strategy to develop cost-effective electrocatalysts from industrial alloys. The scalability, speed, and versatility of laser processing, offer practical pathways for manufacturing large-scale water splitting electrodes for hydrogen production technologies.

CRediT authorship contribution statement

Angelja Kjara Surca: Writing – review & editing, Writing – original draft, Methodology, Funding acquisition, Formal analysis, Data curation. **Marjan Bele:** Formal analysis, Data curation. **Črtomir Donik:** Formal analysis, Data curation. **Irena Paulin:** Formal analysis, Data curation. **Martin Šala:** Formal analysis, Data curation. **Jakob Starec Oman:** Formal analysis. **Miha Osredkar:** Formal analysis. **Mejrema Nuhanović:** Formal analysis, Data curation. **Jan Ocepek:** Formal analysis, Data curation. **Matjaž Godec:** Funding acquisition. **Goran Dražič:** Methodology, Formal analysis, Data curation. **Nejc Hodnik:** Methodology, Funding acquisition. **Luka Suhadolnik:** Writing – review & editing, Writing – original draft, Methodology, Funding acquisition, Conceptualization.

Declaration of competing interest

The authors declare that they have no known competing financial interests or personal relationships that could have appeared to influence the work reported in this paper.

Acknowledgments

N.H. acknowledges the European Research Council (ERC) for the Starting Grant 123STABLE (Grant agreement ID: 852208). The provision of financial support for the research and the preparation of the manuscript by the Slovenian Research and Innovation Agency (ARIS) within the research programs P2-0421P1-0034, P2-0393, P2-0082 and P2-0118 and the projects MN-0022, N2-0155, J2-3041, J1-4401, N2-0248, J7-50227, J7-4636, J2-50058, and J2-50076 is gratefully acknowledged. Views and opinions expressed are however those of the authors only and do not necessarily reflect those of the Republic of Slovenia, ARIS, the European Union, or the European Commission. Neither the Republic of Slovenia, ARIS, the European Union nor the European Commission can be held responsible for them. The authors would also like to thank Matjaž Finšgar (Faculty of Chemistry and Chemical Engineering, University of Maribor, Slovenia) for performing the XPS and ToF-SIMS analyses. Special thanks to our student Vid Pungerčar for his dedication to work.

Appendix A. Supplementary data

Supplementary data to this article can be found online at https://doi.org/10.1016/j.ijhydene.2025.153321.

References

[1] Katsounaros I, Cherevko S, Zeradjanin AR, Mayrhofer KJJ. Oxygen electrochemistry as a cornerstone for sustainable energy conversion. Angew Chem Int Ed 2014;53:102–21. https://doi.org/10.1002/anie.201306588.
[2] Charles V, Anumah AO, Adegoke KA, Adesina MO, Ebuka IP, Gaya NA, et al. Progress and challenges pertaining to the earthly-abundant electrocatalytic materials for oxygen evolution reaction. Sustain Mater Technol 2021;28:e00252. https://doi.org/10.1016/j.susmat.2021.e00252.
[3] Diaz-Morales O, Ferrus-Suspedra D, Koper MTM. The importance of nickel oxyhydroxide deprotonation on its activity towards electrochemical water oxidation. Chem Sci 2016;7:2639–45. https://doi.org/10.1039/c5sc04486c.
[4] Fukushima T, Tsuchimoto K, Oyamada N, Sato D, Minamimoto H, Murakoshi K. Raman spectroscopic observation of electrolyte-dependent oxygen evolution reaction intermediates in nickel-based electrodes. J Phys Chem C 2024;128:20156–64. https://doi.org/10.1021/acs.jpcc.4c06732.
[5] Klaus S, Cai Y, Louie MW, Trotochaud L, Bell AT. Effects of Fe electrolyte impurities on $Ni(OH)_2$/NiOOH structure and oxygen evolution activity. J Phys Chem C 2015;119:7243–54. https://doi.org/10.1021/acs.jpcc.5b00105.
[6] Louie MW, Bell AT. An investigation of thin-film Ni–Fe oxide catalysts for the electrochemical evolution of oxygen. J Am Chem Soc 2013;135:12329–37. https://doi.org/10.1021/ja405351s.
[7] Xie Y, Xu S, Meng AC, Zheng B, Chen Z, Tour JM, et al. Laser-induced high-entropy alloys as long-duration bifunctional electrocatalysts for seawater splitting. Energy Environ Sci 2024;17:8670–82. https://doi.org/10.1039/d4ee01093k.
[8] Gabler A, Müller CI, Rauscher T, Köhring M, Kieback B, Röntzsch L, et al. Ultrashort pulse laser-structured nickel surfaces as hydrogen evolution electrodes for alkaline water electrolysis. Int J Hydrogen Energy 2017;42:10826–33. https://doi.org/10.1016/j.ijhydene.2017.02.006.
[9] Tang T, Jiao S, Han J, Wang Z, Guan J. Partially crystallized Ni–Fe oxyhydroxides promotes oxygen evolution. Int J Hydrogen Energy 2023;48:5774–82. https://doi.org/10.1016/j.ijhydene.2022.11.118.
[10] Yang M, Zhu H, Zheng Y, Zhang C, Luo G, Xu Q, et al. One-step chemical vapor deposition fabrication of ni@nio@graphite nanoparticles for the oxygen evolution reaction of water splitting. RSC Adv 2022;12:10496–503. https://doi.org/10.1039/D2RA00947A.
[11] Kong Q, Wang J, Liu Z, Wu S, Tong X, Zong N, et al. One-step electrodeposition of V-doped NiFe nanosheets for low-overpotential alkaline oxygen evolution. Dalton Trans 2023;52:16963–73. https://doi.org/10.1039/D3DT03066K.
[12] Liu Q, Wang Y, Lu X. Construction of NiFe-Layered double hydroxides arrays as robust electrocatalyst for oxygen evolution reaction. Catalysts 2023;13:586. https://doi.org/10.3390/catal13030586.
[13] Conradi M, Kocijan A, Podgornik B. Enhancing magnesium bioactivity for biomedical applications: effects of laser texturing and sandblasting on surface properties. Materials 2024;17:4978. https://doi.org/10.3390/ma17204978.
[14] Miao J, Li T, Li Q, Chen X, Ren Z, Lu Y. Enhanced surface properties of the Al0.65CoCrFeNi high-entropy alloy via laser remelting. Materials 2023;16:1085. https://doi.org/10.3390/ma16031085.
[15] Sota K, Mondal S, Ando K, Uchimoto Y, Nakajima T. Nanosecond laser texturing of Ni electrodes as a high-speed and cost-effective technique for efficient hydrogen evolution reaction. Int J Hydrogen Energy 2024;93:1218–26. https://doi.org/10.1016/j.ijhydene.2024.10.389.
[16] Ou G, Fan P, Zhang H, Huang K, Yang C, Yu W, et al. Large-scale hierarchical oxide nanostructures for high-performance electrocatalytic water splitting. Nano Energy 2017;35:207–14. https://doi.org/10.1016/j.nanoen.2017.03.049.
[17] Jeyaprakash N, Yang C-H, Prabu G, Clinktan R. Microstructure and tribological behaviour of Inconel-625 superalloy produced by selective laser melting. Met Mater Int 2022;28:2997–3015. https://doi.org/10.1007/s12540-022-01198-5.
[18] Skobir Balantič DA, Donik Č, Podgornik B, Kocijan A, Godec M. Improving the surface properties of additive-manufactured Inconel 625 by plasma nitriding. Surf

Coating Technol 2023;452:129130. https://doi.org/10.1016/j.surfcoat.2022.129130.
[19] Karthik D, Arul Xavier Stango S, Vijayalakshmi U, Swaroop S. Electrochemical behavior of laser shock peened Inconel 625 superalloy. Surf Coating Technol 2017;311:46–54. https://doi.org/10.1016/j.surfcoat.2016.12.105.
[20] Sarkar A, Mukherjee P, Barat P, Jayakumar T, Mahadevan S, Rai SK. Lattice misfit measurement in inconel 625 by X-ray diffraction technique. Int J Mod Phys B 2008;22:3977–85. https://doi.org/10.1142/S0217979208048772.
[21] Nguejio J, Szmytka F, Hallais S, Tanguy A, Nardone S, Godino Martinez M. Comparison of microstructure features and mechanical properties for additive manufactured and wrought nickel alloys 625. Mater Sci Eng 2019;764:138214. https://doi.org/10.1016/j.msea.2019.138214.
[22] Li S, Wei Q, Shi Y, Zhu Z, Zhang D. Microstructure characteristics of inconel 625 superalloy manufactured by selective laser melting. J Mater Sci Technol 2015;31:946–52. https://doi.org/10.1016/j.jmst.2014.09.020.
[23] Garcia-Miranda Ferrari A, Crapnell RD, Adarakatti PS, Suma BP, Banks CE. Electroanalytical overview: the detection of chromium. Sens Acutators Rep 2022;4:100116. https://doi.org/10.1016/j.snr.2022.100116.
[24] Yeo BS, Bell AT. In situ raman Study of nickel oxide and gold-supported nickel oxide catalysts for the electrochemical evolution of oxygen. J Phys Chem C 2012;116:8394–400. https://doi.org/10.1021/jp3007415.
[25] Garcia AC, Touzalin T, Nieuwland C, Perini N, Koper MTM. Enhancement of oxygen evolution activity of nickel oxyhydroxide by electrolyte alkali cations. Angew Chem Int Ed 2019;58:12999–3003. https://doi.org/10.1002/anie.201905501.
[26] Jiang Q, Wang S, Zhang C, Sheng Z, Zhang H, Feng R, et al. Active oxygen species mediate the iron-promoting electrocatalysis of oxygen evolution reaction on metal oxyhydroxides. Nat Commun 2023;14. https://doi.org/10.1038/s41467-023-42646-z.
[27] Jing C, Li L, Chin Y-Y, Pao C-W, Huang W-H, Liu M, et al. Balance between Fe^{IV}–Ni^{IV} synergy and lattice oxygen contribution for accelerating water oxidation. ACS Nano 2024;18:14496–506. https://doi.org/10.1021/acsnano.4c01718.
[28] Suzuki A, Yaita K, Verma G, Jerkiewicz G, Tryk DA, Kuzume A. *In Situ* shell-isolated nanoparticle-enhanced raman spectroscopy Study of nickel surface oxides reveals previously unseen surface chemical dynamics. ACS Electrochem 2025;1:873–85. https://doi.org/10.1021/acselectrochem.4c00202.
[29] Zhang L, Wang L, Holt CMB, Navessin T, Malek K, Eikerling MH, et al. Oxygen reduction reaction activity and electrochemical stability of thin-film bilayer systems of platinum on niobium oxide. J Phys Chem C 2010;114:16463–74. https://doi.org/10.1021/jp104306j.
[30] Zheng J-X, OuYang S-Q, Feng L, Sun J-J, Xuan Z-W, Fang J-H. In-situ Raman spectroscopic studies on electrochemical oxidation behavior of chromium in alkaline solution. J Electroanal Chem 2022;921:116682. https://doi.org/10.1016/j.jelechem.2022.116682.
[31] Biesinger MC, Payne BP, Grosvenor AP, Lau LWM, Gerson AR, Smart RStC. Resolving surface chemical states in XPS analysis of first row transition metals, oxides and hydroxides: cr, Mn, Fe, Co and Ni. Appl Surf Sci 2011;257:2717–30. https://doi.org/10.1016/j.apsusc.2010.10.051.
[32] Grosvenor AP, Biesinger MC, Smart RStC, McIntyre NS. New interpretations of XPS spectra of nickel metal and oxides. Surf Sci 2006;600:1771–9. https://doi.org/10.1016/j.susc.2006.01.041.
[33] Wu X, Voyshnis S, Seyeux A, Chumlyakov Y, Marcus P. ToF-SIMS study of oxide films thermally grown on nickel-base alloys. Corros Sci 2018;141:175–81. https://doi.org/10.1016/j.corsci.2018.06.043.
[34] Mazenc A, Galtayries A, Seyeux A, Marcus P, Leclercq S. ToF-SIMS study of the behavior of thermally oxidized films formed on nickel-based 690 alloy in high-temperature water. Surf Interface Anal 2013;45:583–6. https://doi.org/10.1002/sia.5060.
[35] Voyshnis S, Seyeux A, Zanna S, Martin-Cabanas B, Couvant T, Marcus P. Oxide layer growth on nickel-base alloy surfaces in high temperature water and in O2 studied by ToF-SIMS with isotopic tracers. Corros Sci 2018;145:212–9. https://doi.org/10.1016/j.corsci.2018.10.009.
[36] Cordoba-Torresi SI, Hugot-Le Goff A, Joiret S. Electrochromic behavior of nickel oxide electrodes: II . Identification of the bleached State by raman spectroscopy and nuclear reactions. J Electrochem Soc 1991;138:1554–9. https://doi.org/10.1149/1.2085831.
[37] Mavrič A, Fanetti M, Lin Y, Valant M, Cui C. Spectroelectrochemical tracking of nickel hydroxide reveals its irreversible Redox States upon operation at high Current density. ACS Catal 2020;10:9451–7. https://doi.org/10.1021/acscatal.0c01813.
[38] Maslar JE, Hurst WS, Bowers WJ, Hendricks JH, Aquino MI, Levin I. In situ Raman spectroscopic investigation of chromium surfaces under hydrothermal conditions. Appl Surf Sci 2001;180:102–18. https://doi.org/10.1016/s0169-4332(01)00338-5.
[39] De Faria DLA, Venâncio Silva S, De Oliveira MT. Raman microspectroscopy of some iron oxides and oxyhydroxides. J Raman Spectrosc 1997;28:873–8. https://doi.org/10.1002/(sici)1097-4555(199711)28:11%253C873::aid-jrs177%253E3.0.co;2-b.
[40] Dieterle M, Weinberg G, Mestl G. Raman spectroscopy of molybdenum oxides. Phys Chem Chem Phys 2002;4:812–21. https://doi.org/10.1039/b107012f.
[41] Jehng JM, Wachs IE. Structural chemistry and Raman spectra of niobium oxides. Chem Mater 1991;3:100–7. https://doi.org/10.1021/cm00013a025.
[42] Trotochaud L, Young SL, Ranney JK, Boettcher SW. Nickel–Iron oxyhydroxide oxygen-evolution electrocatalysts: the role of intentional and incidental iron incorporation. J Am Chem Soc 2014;136:6744–53. https://doi.org/10.1021/ja502379c.
[43] Trześniewski BJ, Diaz-Morales O, Vermaas DA, Longo A, Bras W, Koper MTM, et al. In situ observation of active oxygen species in Fe-Containing Ni-Based oxygen evolution catalysts: the effect of pH on electrochemical activity. J Am Chem Soc 2015;137:15112–21. https://doi.org/10.1021/jacs.5b06814.
[44] Lee S, Chu Y-C, Bai L, Chen HM, Hu X. Operando identification of a side-on nickel superoxide intermediate and the mechanism of oxygen evolution on nickel oxyhydroxide. Chem Catal 2023;3:100475. https://doi.org/10.1016/j.checat.2022.11.014.
[45] Šurca A, Orel B, Pihlar B, Bukovec P. Optical, spectroelectrochemical and structural properties of sol-gel derived Ni-oxide electrochromic film. J Electroanal Chem 1996;408:83–100. https://doi.org/10.1016/0022-0728(96)04509-3.
[46] Gallenberger J, Moreno Fernández H, Alkemper A, Li M, Tian C, Kaiser B, et al. Stability and decomposition pathways of the NiOOH OER active phase of NiO_x electrocatalysts at open circuit potential traced by *ex situ* and *in situ* spectroscopies. Catal Sci Technol 2023;13:4693–700. https://doi.org/10.1039/D3CY00674C.

Update

International Journal of Hydrogen Energy
Volume 205, Issue , 30 January 2026, Page

DOI: https://doi.org/10.1016/j.ijhydene.2026.153538

International Journal of Hydrogen Energy 205 (2026) 153538

Contents lists available at ScienceDirect

International Journal of Hydrogen Energy

journal homepage: www.elsevier.com/locate/he

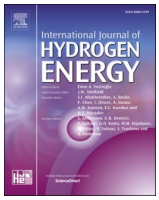

Corrigendum

Corrigendum to 'Laser-engineered Inconel 625 for enhanced oxygen evolution electrocatalysis' [Int J Hydrogen Energy (2026) 1–11/153321]

Angelja Kjara Surca [a,*], Marjan Bele [a], Črtomir Donik [b], Irena Paulin [b], Martin Šala [c], Jakob Starec Oman [a], Miha Osredkar [a], Mejrema Nuhanović [a], Jan Ocepek [a], Matjaž Godec [b], Goran Dražič [a], Nejc Hodnik [a,b], Luka Suhadolnik [a,**]

[a] Department of Materials Chemistry, National Institute of Chemistry, Hajdrihova 19, SI-1000, Ljubljana, Slovenia
[b] Institute of Metals and Technology, Lepi pot 11, SI-1000, Ljubljana, Slovenia
[c] Department of Analytical Chemistry, National Institute of Chemistry, Hajdrihova 19, SI-1000, Ljubljana, Slovenia

The authors regret that some funding sources were incorrectly listed during the proof-reading stage. Please note that these changes do not affect the results or conclusions of the study. The authors would like to apologise for any inconvenience caused.

Corrigendum to Acknowledgements

The provision of financial support for the research and the preparation of the manuscript by the Slovenian Research and Innovation Agency (ARIS) within the research programs P1-0034, P2-0132, P2-0393, P2-0421 and I0-0003 and the projects GC-0001, GC-0003, GC-0004, MN-0022, N2-0155, N2-0248, N2-0425, J2-3041, J1-4401, J7-4636, and J2-50076 is gratefully acknowledged. The authors acknowledge partial support from the Republic of Slovenia, the Ministry of Higher Education, Science and Innovation, and the European Union – NextGenerationEU in the framework of the project HyBReED, part of the Slovenian Recovery and Resilience Plan. Views and opinions expressed are however those of the authors only and do not necessarily reflect those of the Republic of Slovenia, the Ministry of Higher Education, the European Union, or the European Commission. Neither the Republic of Slovenia, the Ministry of Higher Education, Science and Innovation, the European Union nor the European Commission can be held responsible for them. The authors would also like to thank Matjaž Finšgar (Faculty of Chemistry and Chemical Engineering, University of Maribor, Slovenia) for performing the XPS and ToF-SIMS analyses. This project is co-financed by the Republic of Slovenia, the Ministry of Education, Science and Sport, and the European Union under the European Regional Development Fund. Special thanks to our student Vid Pungerčar for his dedication to work. N.H. acknowledges the European Research Council (ERC) for the Starting Grant 123STABLE (Grant agreement ID: 852208) and the North Atlantic Treaty Organization Science for Peace and Security (NATO SPS) programme (grant G6230).

DOI of original article: https://doi.org/10.1016/j.ijhydene.2025.153321.
* Corresponding author.
** Corresponding author.
E-mail addresses: angelja.k.surca@ki.si (A.K. Surca), luka.suhadolnik@ki.si (L. Suhadolnik).

https://doi.org/10.1016/j.ijhydene.2026.153538

Available online 14 January 2026